

## A Multipurpose Scanning Spectral Polarimeter (SSP): Instrument Description and Sample Results

GRAEME L. STEPHENS, ROBERT F. MCCOY JR., RENATA B. MCCOY, PHILIP GABRIEL,  
PHILIP T. PARTAIN, AND STEVEN D. MILLER

*Department of Atmospheric Science, Colorado State University, Fort Collins, Colorado*

STEVEN P. LOVE

*Space and Remote Sensing Sciences Group, Los Alamos National Laboratory, Los Alamos, New Mexico*

(Manuscript received 24 November 1998, in final form 2 July 1999)

### ABSTRACT

This paper describes the design and characteristics of a scanning spectral polarimeter designed to measure spectral radiances and fluxes in the range between 0.4 and 4.0  $\mu\text{m}$ . The instrument characteristics are described, and the procedures to calibrate the unpolarized radiances and fluxes in the spectral range from 0.4 to 1.1  $\mu\text{m}$  are discussed along with detailed error analyses of this calibration. The accuracy of the radiance calibration was determined to be approximately 3%. The calibration of fluxes based on two different procedures is estimated to be accurate to 3%–6%. Detailed calibration of fluxes was performed using a standard lamp that is not an isotropic source. For this type of calibration the angular response of the flux channel deviates from a pure cosine function at wavelengths longer than 0.74  $\mu\text{m}$ , thus forming a frontal lobe. A less detailed calibration using a 40-in. integrated sphere was also performed. In that case the light source is isotropic and the frontal lobe does not appear. Calibration factors are derived by combining data from both calibration procedures. A comparison with spectral flux measurements obtained from different instruments with different angular response properties is presented with agreement that is within the quoted calibration accuracy. Measurements obtained from two different aircraft flights are presented to illustrate the types of application of the data. Data analyses shows that the reflected (unpolarized) fluxes measured above a cirrus cloud can be reasonably matched to modeled fluxes using optical properties retrieved from the measured (unpolarized) radiances.

### 1. Introduction

Understanding the transfer of solar radiation in the earth's atmosphere is important for a number of reasons. Differential absorption of solar radiation at the surface fuels the circulation of the oceans. Absorption of solar radiation in the atmosphere is likewise an important source of energy for the large-scale circulation of the atmosphere. The variation of the fluxes of solar radiation are primarily affected by clouds, and to a lesser extent by aerosol.

The detailed nature of the transfer of solar radiation in clouds has recently been called into question (e.g., Cess et al. 1995; Pilewskie and Valero 1995; Valero et al. 1997a,b). These studies are based on the interpretation of heterogeneous datasets and debate about the validity of these interpretations lingers (e.g., Stephens

1996; Barker and Li 1997). One reason this debate endures is that there is a general lack of high quality observations of solar fluxes in and around clouds. This lack of data was one of the main motivations for the development of a spectrometer more than a decade ago by the principle author of this paper (Stephens and Scott 1985; Scott and Stephens 1985). The instrument described in this paper, the Scanning Spectral Polarimeter (SSP), is a third-generation version of this earlier instrument.

The purpose of this paper is to provide a description of the design of the SSP, present details about the calibration procedure used, and provide examples of data obtained during a number of aircraft measurements campaigns carried out by the U.S. Department of Energy (DOE) Atmospheric Radiation Measurement (ARM) Unmanned Aerospace Vehicle (UAV) program (e.g., Valero et al. 1996 and available online at <http://armuav.atmos.colostate.edu/armuav.html>). The version of the SSP described in this paper has six channels, four of which are devoted to measurement of the linear and circular polarization, although the measurements obtained with these polarization channels are not reported

---

*Corresponding author address:* Dr. Graeme L. Stephens, Department of Atmospheric Science, Colorado State University, Fort Collins, CO 80523-1371.  
E-mail: [stephens@atmos.colostate.edu](mailto:stephens@atmos.colostate.edu)

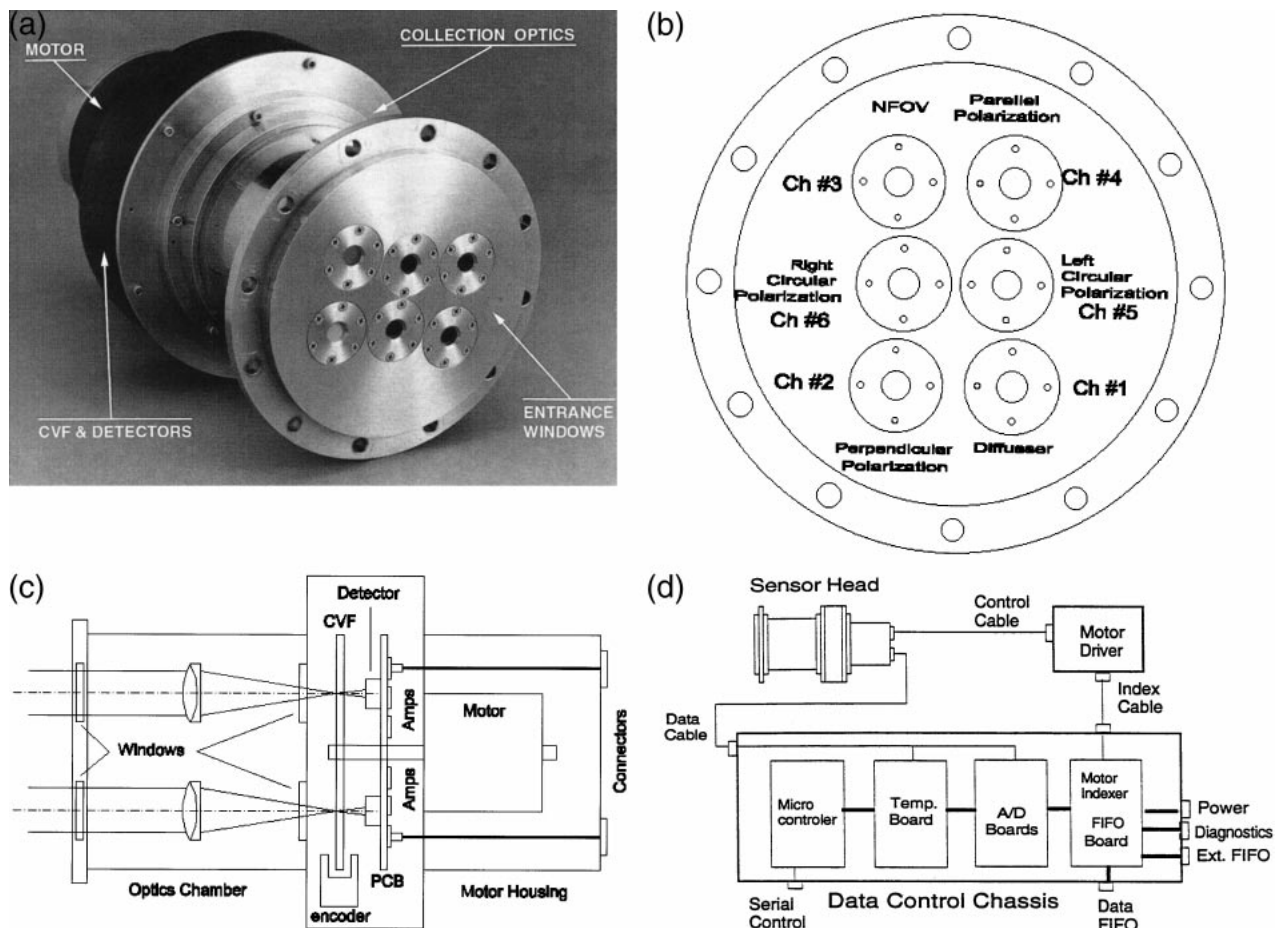


FIG. 1. (a) The SSP instrument showing the main components of the sensor and the overall size of the instrument. (b) The front view showing the six entrance windows to the instrument for the six channels. (c) An expanded view of the optical layout of the SSP instrument. (d) A schematic diagram of the data acquisition system.

in this paper and will be the topic of a future paper. The focus of the paper is on the measurements provided by the remaining two channels of the instrument. One channel measures the spectral (unpolarized) radiance (hereafter referred to as channel 3) and the other channel measures the spectral flux (channel 1). The main optical component of the instrument is a circular variable filter that provides measurements of these radiances and fluxes in the spectral region from 0.4 to 4.0  $\mu\text{m}$  (although only measurements in the region between 0.4 and 1.1  $\mu\text{m}$  are presented in this paper).

The outline of the paper is as follows. The design and characteristics of the instrument are summarized in the following two sections. Section 4 provides a detailed discussion of the instrument calibration, which also includes an error analysis of the calibration procedure. The calibration is shown to be robust, and the instrument has remained stable in its performance over a period of more than two years. Section 5 provides a comparison of SSP measurements with measurements obtained using different instruments that provide similar information. Section 6 presents selected results obtained from

field experiments. The final section summarizes the key results of the paper.

## 2. Instrument design and characteristics

One of the main design features of the SSP is its modularity. The instrument consists of three principal components (see Fig. 1a)—the motor driver assembly, a filter wheel and detector assembly, and the optical assembly. The optical assembly is held in a vacuum to reduce the hazard of thermal shock to the polarization optics and to reduce the possibility of any condensation on the optical surfaces. The modular feature of the instrument provides a number of advantages, including the ability to use different optical assemblies (such as with or without polarization optics) or different filter arrangements. A more detailed discussion of each of these main components is now presented.

### a. The optical assembly

The optical assembly is a vacuum chamber with entrance and exit windows. There are six separate light

paths within the optical assembly, as indicated by the layout of the six entrance windows of Figs. 1a,b. These define the six different channels of the instrument. The optics are mounted in a tower assembly attached to the rear of the optical assembly. This tower has three layers of optics. The first layer contains two Fresnel Rhombus for channels 5 and 6. The second layer contains four Glan Taylor polarizing cubes for the discerning linear polarization for channels 2 and 4 and to differentiate between left circular and right circular polarization in channels 5 and 6. The third layer consists of focusing optics, five of which are achromatic. Sunlight then exits this assembly to the filter. Figure 1c provides a schematic of the mechanical layout of the instrument and the optical layout of one channel of the instrument.

A multispectral grade of zinc sulfide (ZnS) is used for the entrance and exit windows and the focusing lens of the narrow field-of-view (FOV) channel. The four polarization channels employ borosilicate crown glass (BK-7) for the windows, and the hemispheric flux channel (channel 1) uses a flashed opal diffuser on a BK-7 substrate as the cosine receptor and BK-7 for the exit window. The practical wavelength range of any given channel of the instrument is determined by the optical material used in the optical configuration of that channel. The BK-7 and calcite polarizing cubes limits the range to  $2.5 \mu\text{m}$ , whereas the ZnS transmits beyond  $4.0 \mu\text{m}$ , which is the upper range of the filters and detectors used by the instrument. This effectively limits all polarization and flux information to wavelengths below  $2.5 \mu\text{m}$ , whereas the radiance information can, in principle, be obtained up to  $4.0 \mu\text{m}$ .

#### *b. The filter assembly*

The filter assembly consists of a circular variable filter (CVF), which is constructed in four  $90^\circ$  segments. This filter has a continuously variable bandpass across the spectral range from  $0.38$  to  $4.0 \mu\text{m}$ . The first two segments of the filter are made from BK-7 substrates with the thin film mounted between two plates. The remaining two segments are constructed on silicon (Si) with films applied to the outer surfaces.

The four segments of the filter are mounted in an aluminum wheel with a 1-mm spacing between segments, providing a clear aperture for broadband measurements. An optical encoder is located on the outer rim of the wheel holding the CVF and provides the locations of the central wavelengths of the measurements recorded by the detector. The encoder also provides information that indicates the start of a scan. Light from the optical assembly is focused onto the CVF wheel and reexpanded onto the detectors after passing through a field stop. The wider the beam on the CVF, the wider the bandwidth. Since refractive optics were used, the near-infrared radiation focuses to a different spot size than does visible radiation. The bandwidths of

the instrument were derived from the calibration procedure described below.

Only measurements obtained from the first two segments of the wheel, that is, over the spectral range between 400 and 1100 nm, are reported in this paper. A total of 107 measurements are recorded around the entire filter wheel and 55 of these measurements are located within the two segments that represent this spectral range. Excluding the edges of segments of the filter wheel where overlap occurs, this leads to measurements at approximately 45 wavelengths between 400 and 1100 nm. The spectral resolution associated with these measurements is characterized by the filter half-bandwidth that ranges from 12 nm at the shorter wavelengths to 17 nm for the longer wavelengths.

#### *c. The detector assembly*

Although the detector used in the version of the instrument reported in this paper consists of a two-color hybrid assembly, which has a photovoltaic Si element mounted over a photoconductive lead selenide (PbSe) element, only the Si detector was calibrated. This detector was integrated with two hybrid preamplifiers into a TO-8 package in close proximity to the detectors.

#### *d. The sensor and data acquisition system*

The CVF is rotated by a stepper motor up to a rate of 10 revolutions per second (that is up to 10 spectral scans per second). This rate of rotation can be selected and controlled by the computer control system. The data reported in this paper were obtained with the stepper motor rotating at a rate of two revolutions per second. This rate of scanning was limited by the real-time telemetry system on the aircraft platform. The only electronics on the sensor head are the preamplifiers mounted on each detector.

Figure 1d provides a schematic diagram of the data acquisition system. The main components are (i) four analog-to-digital (A/D) boards that have four 16-bit sample-and-hold channels with digital gain control, the first 12 of these 16 channels acquire the optical data and the remaining 4 channels acquire temperature and other system data; (ii) a temperature board that provides information obtained from resistive thermal devices (RTDs) imbedded in the sensor head; (iii) an indexer board that steps the motor; and (iv) the CPU board that controls data ingest, monitors instrument status, and provides other control features (such as gain settings and rotation rate of the filter wheel, among others). This CPU board contains a standard 8051 microcontroller and also two  $8 \text{ K} \times 9$  bit FIFOs (first in–first out) for data output. A real-time clock provides a time stamp at the beginning of each scan.

The scan procedure begins with the start of the scan bit signal received from the sensor head. The 8051 writes a header to the FIFO. This header contains a time

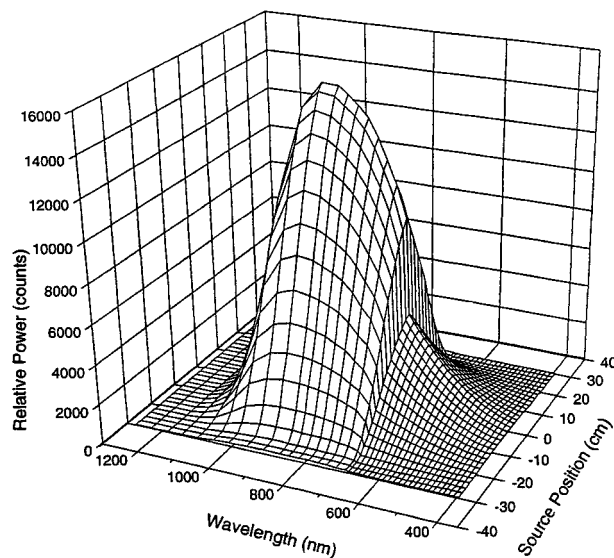


FIG. 2. Relative intensity vs wavelength and position of the light source relative to the central axis of the instrument. The FOV is close to a Gaussian function, and the jump in received intensity at 700 nm is a feature of the difference in transmission of two different segments of the filter wheel. The source position of 10 cm defined relative to a central axis corresponds to an angle of  $0.9^\circ$ .

stamp, gain settings, motor speed, and RTD temperature measurements. The controller then waits for a valid data bit signal from the sensor. Each time this data bit is detected, the processor collects all 12 optical channels of 16-bit A/D data and sends these to the FIFO. This process is repeated to obtain 107 spectral data measurements around the rotating filter wheel. The recording of a header and 107 spectral measurements per channel comprises one scan. More details of the instrument operation are given in the SSP home page, which is available online at <http://optical.atmos.colostate.edu>.

### 3. Instrument characteristics

#### a. Radiance channel field of view

The FOV of the SSP instrument was determined using the following setup. The SSP and a light source were mounted on separate platforms approximately 6 m apart. The light source, shielded to prevent stray light from reaching the SSP, was then moved across the SSP field of view and the distance of the source from the optical axis of the instrument was measured. Data were then acquired as a function of this distance, and the results of the analyses of the data are presented in Fig. 2. The scans for the wavelengths range from 400 to 700 nm are taken through one-quarter of the CVF wheel, and the scans for the 700–1100-nm range derive from transmission through another quarter of the CVF wheel. The slightly different properties of each sector of the filter wheel produce the observed discontinuity in the 3D surface around 700 nm. The measured half-angle FOV of

channel 3 is 20 mrad and is practically invariant with wavelength.

#### b. Flux channel cosine response to a standard lamp light source

The entrance window of channel 1 is constructed with a commercially available flashed opal diffuser. This material is used to collect hemispheric radiation, thus providing a measure of hemispheric flux. The angular response of this channel was assessed using a setup similar to that used to determine the FOV of channel 3. In this case, however, the light source from a calibrated standard lamp was held in a fixed position and the SSP was rotated in  $0.25^\circ$  steps from  $-1^\circ$  to  $+4^\circ$  from the optical axis of the instrument. This small increment in rotation was chosen to help map out the shape of any frontal transmission features of the diffuser. Several hundred scans were acquired at each angle before rotating the SSP to the next angle. The SSP was then rotated in  $5^\circ$  increments from  $5^\circ$  to  $65^\circ$  and then in  $1^\circ$  increments beyond  $65^\circ$ .

Figure 3a presents the angular response of the SSP as a function of the incident angle and wavelength of radiation received from the standard lamp. The ideal cosine response is maintained within less than 3% for all wavelengths over the range of angles  $2^\circ < \theta < 40^\circ$ , between 3% to 20% for  $40^\circ < \theta < 60^\circ$ , and begins to deviate significantly from the ideal cosine response for angles larger than  $60^\circ$ . There are also no appreciable frontal transmission lobes in the visible region, but undesirable forward transmission features occur at near-infrared wavelengths (larger than about 740 nm), as shown in Fig. 3b. The frontal transmission lobes appear only for angles from  $-2^\circ$  to  $2^\circ$  and are absent if the light is a true isotropic source. These lobes will be a source of measurement error especially when SSP views a highly anisotropic light source, such as under clear-sky conditions looking toward the zenith sky. The measurements described in this paper apply to the instrument mounted in the nadir position measuring diffuse light—conditions that should minimize affects of frontal transmission lobes. This assumption is also supported by the comparisons of spectral fluxes obtained by the SSP and different instruments with different angular responses discussed later.

#### c. Dark currents and offsets

One of the features of the SSP is its ability to measure any dark currents (DCs) and DC offsets on every scan. When the infrared portion of the circular variable filter is over the visible silicon detector the signal is blocked and the data are averaged to determine the DC offsets. This procedure is carried out as part of the data post-processing.

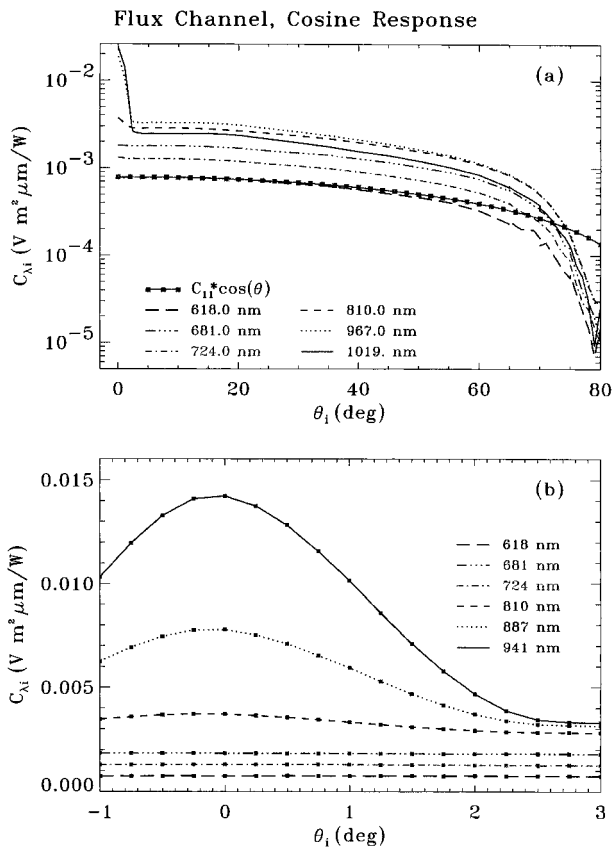


FIG. 3. (a) Illustration of the cosine response of channel 1 of the instrument for selected wavelengths. Comparison of the cosine response for the 618-nm wavelength with the pure cosine response is also shown. (b) Example of the frontal transmission lobes between  $-2^\circ$  and  $2^\circ$  from instrument normal for wavelengths greater than 740 nm in response to an anisotropic light source.

#### 4. Instrument calibration

The instrument has undergone extensive calibration both at the Sandia National Laboratory (SNL) and the Los Alamos National Laboratory (LANL) Optical and Infrared Laboratory. LANL also provides calibration services to the ARM/UAV program as a whole as well as participates in other programs (<http://optical.atmos.colostate.edu/lanl1.html>).

##### a. Radiance calibration

The sensor response is obtained by equating the measured output voltage  $V_\lambda$  of the instrument to the known output of the sphere  $I_\lambda$ ,

$$C_\lambda = \frac{V_\lambda}{I_\lambda}, \quad (1)$$

and has units of  $V m^2 sr \mu m W^{-1}$ . A 12-in. Labsphere integrating sphere was used to obtain the calibration factors  $C_\lambda$ . The calibration was performed by mounting the SSP on an optical bench 50 cm from the integrating

sphere. The distance between the SSP and sphere is irrelevant for this particular procedure provided the FOV is maintained within the aperture of the sphere and no stray light enters the instrument from sources other than the sphere. Data for a given channel are averaged over several hundred scans at each gain setting.

The SSP was calibrated in this way under different temperature conditions, and the results of this calibration are presented in Fig. 4a. Figure 4b provides the spectra of  $C_\lambda$  obtained from the calibration procedure carried out at room temperature on three different occasions over the course of two years (1995–96). These results suggest that (i) the detector has a very small temperature sensitivity especially in the region between 0.4 and 0.75  $\mu m$ , and (ii) the calibration over this period of time remained stable. Except for wavelengths beyond 950 nm,  $C_\lambda$  varied by no more than 2% and 4%, respectively, for the visible and near-infrared portions of the spectrum between the three times of calibration.

##### b. Flux calibration

We define the flux calibration factor  $c_\lambda$  such that the voltage measured by the instrument is related to the flux received by the instrument via

$$V_\lambda = c_\lambda F_\lambda. \quad (2)$$

For  $N$  sources of radiation each illuminating the instrument with flux  $F_\lambda$  at an angle  $\theta_i$  it follows that

$$\sum_i^N V_{\lambda,i} = \sum_i^N c_{\lambda,i} F_\lambda, \quad (3)$$

where for an ideal instrument the angular dependence of the calibration factor follows a simple cosine law, namely,

$$c_{\lambda,i} = c_\lambda \cos \theta_i. \quad (4)$$

Under these ideal conditions,

$$\bar{c}_\lambda = \frac{1}{F_\lambda} \frac{\sum_i V_{\lambda,i}}{\sum_i \cos \theta_i}, \quad (5)$$

where  $\bar{c}_\lambda = c_\lambda$ .

Two different approaches were used to determine  $\bar{c}_\lambda$ . The first approach, hereafter referred to as A1-level calibration, was carried by LANL. In this approach, the SSP was mounted on a rotary stage and illuminated by a standard 1000-W lamp. The instrument was rotated relative to this lamp in the manner described above to determine the cosine response of channel 1. Data were averaged over 100–200 scans and taken at each angular position as the instrument was rotated. The averaged calibration factor was obtained by summing the instrument output at each angle  $\theta_i$  according to (5). The results are presented in Fig. 5a and labeled as the A1 level. Figure 5b is the percentage change in this calibration factor that occurred by altering the temperature by  $20^\circ$

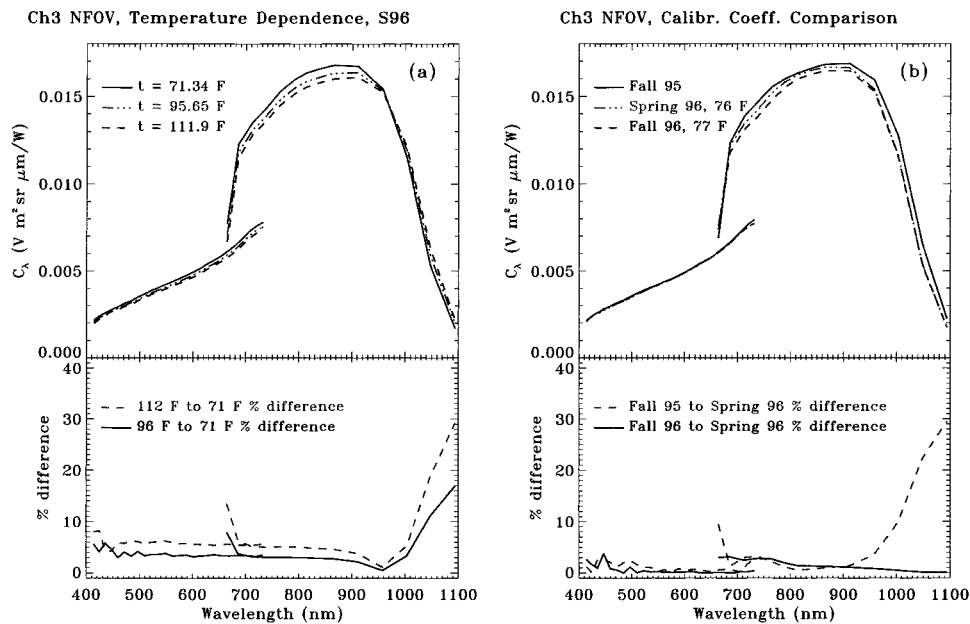


FIG. 4. The spectral calibration coefficient of channel 3 [upper half of both (a) and (b)]. In (a), the calibration is shown for three instrument temperatures and the difference in calibration is presented in the bottom part of the figure. (b) The calibration carried out at three different periods of time and the difference in calibration are shown.

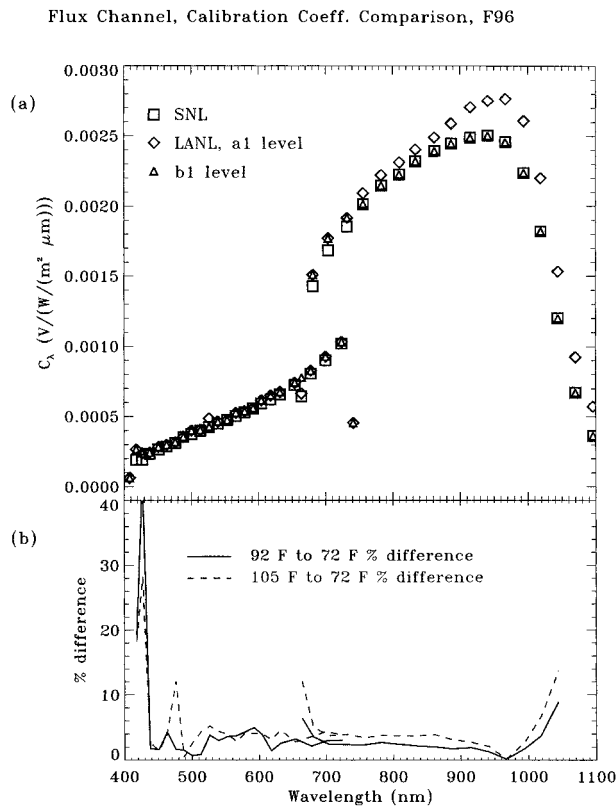


FIG. 5. (a) The calibration factors for channel 1 showing the two calibration approaches described in the text. (b) The change in calibration for given changes in instrument temperature.

and 30°F from room temperature to highlight the relatively small effect that large uncertainties in temperature might introduce to the accuracy calibration.

Figure 5a also contrasts the A1 calibration factors with those obtained from the second calibration procedure carried out at Sandia National Laboratory in Albuquerque, New Mexico (labeled as SNL). This second procedure places the SSP in the aperture of a 40-in. integrating sphere. The sphere is large enough that the FOV of the instrument sees only the radiance field within the sphere. Since this field is isotropic, this approach to calibration is intrinsically less ambiguous than is the A1 calibration method and analyses since the latter analyses are subject to uncertainties associated with the frontal transmission lobes of the diffuser. The calibration coefficient then follows from (2), where  $F_\lambda$  is the isotropic flux output of the sphere. The coefficients obtained in this way are also shown in Fig. 5a. The results highlight the closeness of both calibration procedures for visible wavelengths, which essentially confirms the reasonableness of the cosine response in this spectral region.

The comparison between the two calibration factors also exposes deviations between the two approaches at longer near-infrared wavelengths. The difference between the two calibration factors for wavelengths longer than about 740 nm is a result of the approximate nature of (4) at those wavelengths where significant noncosine response properties of the instrument are observed. In this case, the differences between the A1 calibration and the SNL calibration that occur at the longer wavelengths

are a result of the forward transmission lobe of the diffuser at these wavelengths.

The operational calibration factors applied to the data and referred to as B1-level calibration data are obtained as a combination of the A1 data up to 740 nm and the SNL calibration data at wavelengths beyond 740 nm. It should also be noted that the undesirable features of the diffusing optics also means that the accuracy of the B1 calibration estimated below, in principle, applies only to isotropic incident light sources.

### c. Estimation of calibration accuracy

With cosine response errors aside, there are a number of other sources of uncertainty that contribute to the calibration error of the flux channel. It follows from (5) that

$$dc_{\lambda}^2 = \sum_i \left( \frac{\partial c_{\lambda}}{\partial c_{\lambda,i}} \right)^2 (dc_{\lambda,i})^2 + \sum_i \left( \frac{\partial c_{\lambda}}{\partial \theta_i} \right)^2 (d\theta_i)^2 + \sum_i \left( \frac{\partial c_{\lambda}}{\partial T} \right)^2 (dT)^2, \quad (6)$$

where  $c_{\lambda,i} = V_{\lambda,i}/F_{\lambda}$ . The first term represents the combination of calibration source errors (taken to be 2%, as specified by the supplier of the lamp), instrument noise, and error in wavelength assignment. The second term of (6) represents error in the angular position of lamp relative to instrument and the third factor includes errors associated with either improper account of or neglect of the temperature response of the instrument. The total error in measured fluxes is thus governed by the calibration coefficient error defined by (6) as well as additional noise and temperature uncertainties that might arise from payload noise, aircraft vibration, and other platform-related noise. The total error in measurements of radiances is the combination of calibration geometry and lamp errors, and temperature as well as noise uncertainties.

Flux errors are presented in Fig. 6a and the corresponding radiance errors are shown in Fig. 6b. When combining all factors, we note that the calibration accuracy of the flux lies between 3% and 6% over the spectral region from 0.5 to 1.0  $\mu\text{m}$  and increases toward 10% at the ends of the spectral interval at wavelengths shorter than 0.5  $\mu\text{m}$  and up to 1.0  $\mu\text{m}$ . This increase in error is contributed to by increasing instrument noise largely associated with the decreasing sensitivity of the Si detector at these wavelengths.

The sensitivity of the radiance calibration to temperature is highlighted in Fig. 6b showing the calibration errors associated with a 20° and 40° F error in the specification of temperature (or alternatively a difference of 20° and 40° in the temperature of the sensor from normal operating temperature). This is a worst-case scenario for error estimate since the temperatures of the aircraft payload were monitored during flight. For a given temper-

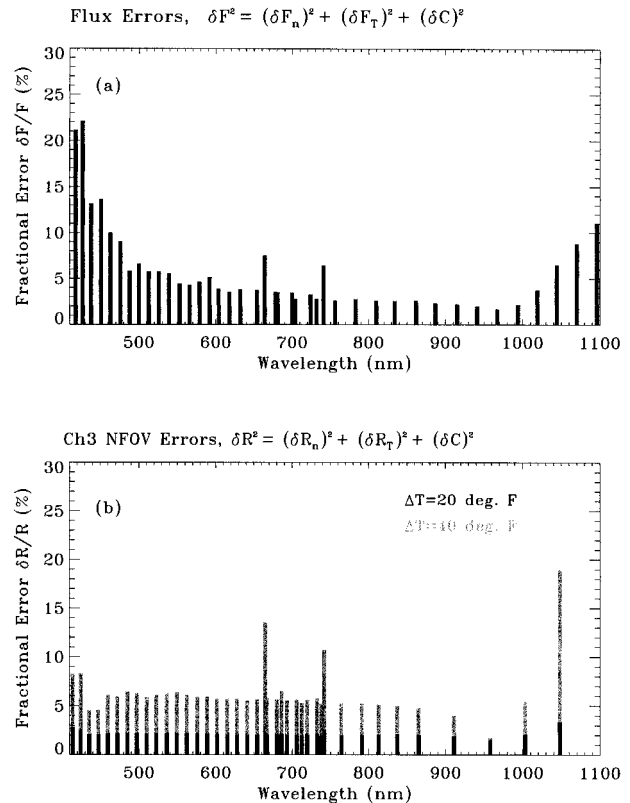


FIG. 6. Derived errors of calibration for channels 1 and 3.

ature uncertainty of 20°F, the radiance channel calibration error is approximately 3% for most of the wavelength range. This level of accuracy is typical of spectrometer measurements of this type (e.g., Chen 1985).

## 5. Comparison of measurements

In this section, calibrated radiances and fluxes obtained by the SSP, mounted on an aircraft and pointed downward, are compared to coincident radiance and fluxes measured by two other instruments that also flew as part of the same airborne payload during a series of flights conducted between 1995 and 1997. One instrument is the Multispectral Pushbroom Imaging Radiometer (MPIR; available online at <http://armuav.atmos.colostate.edu/armuav.html>), which is a filter radiometer that provides spectral radiance data across the track of the aircraft. The second instrument used in the comparison is the Total Diffuse Direct Radiometer (TDDR; Valero et al. 1982), which measures both upwelling and downwelling fluxes in seven spectral channels defined with a bandpass of approximately 10 nm.

Figure 7 provides a comparison of fluxes obtained from two TDDR channels and fluxes obtained from two equivalent spectral bands of the SSP. Although some details of the experiments are given below, it is worth mentioning that the scenes viewed by both sets of instruments varied from thick overcast clouds to broken

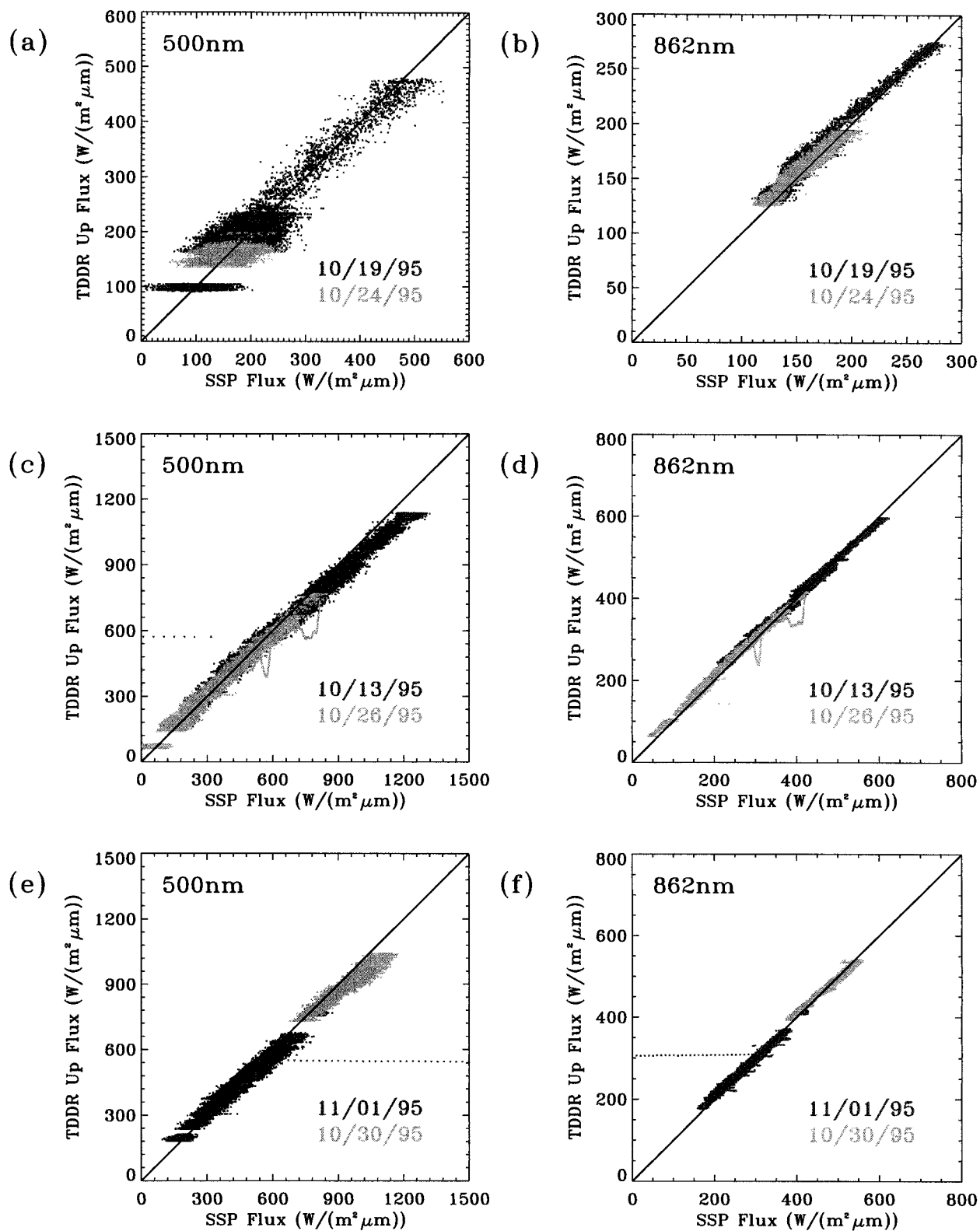


FIG. 7. The comparison between TDDR and SSP 0.5- and 0.862- $\mu m$  spectral fluxes measured from aircraft on the days indicated. The extraneous points off diagonal are an artifact of data interpolation and should be neglected.

clouds, to thin cirrus to clear-sky views of fields surrounding the Southern Great Plains (SGP) site operated by the DOE (Stokes and Schwartz 1994). These scenes provide a variety of different radiance geometries, and thus a comparison between the two instruments provides a way of assessing the possible uncertainty that can be ascribed to the flux calibration of the SSP. The calibrated fluxes of the TDDR were converted to spectral fluxes by dividing these fluxes by the rectangular width of the TDDR spectral response function.

Comparisons are presented for six different flight days including clear-sky scenes (19 and 24 October 1995, Figs. 7a,b), broken cloudy-sky scenes (13 and 26 October 1995, Figs. 7c,d; 1 November 1995, Figs. 7e,f), and an overcast-sky scene (30 October 1995, Figs. 7e,f). These comparisons show a remarkable degree of agreement between the spectral fluxes measured by the SSP and those measured by the TDDR for the range of conditions that represent the measurements. The level of agreement shown is indicative of other flight data not shown. We conclude that the accuracy of the calibration of channel 1 (as stated above) is in fact a robust estimate of calibration accuracy under the range of conditions expected when the SSP views diffusely reflected sunlight.

The second comparison is of SSP radiances with the equivalent spectral radiances measured by the MPIR. The radiances (obtained from the 882-nm channel MPIR, on 30 September and 5 October 1996) are compared in Fig. 8 to the equivalent SSP radiances measured at the same time on these days. The agreement is again excellent even with slightly noisier MPIR radiances.

## 6. Selected examples of measurements

The SSP regularly flies on research aircraft as part of a larger payload developed under the auspices of the DOE ARM UAV program. These campaigns typically deploy two aircrafts and are generally conducted over the SGP ARM site located in Oklahoma and typically occur during spring and fall. The UAV payload consists of a downward-viewing SSP, upward- and downward-viewing TDDRs (Valero and Ackerman 1989) and broadband solar flux radiometers (Valero et al. 1982), a scanning micropulsed cloud lidar, the downlooking MPIR, as well as ancillary in situ probes for temperature and water vapor.

One notable campaign, the Atmospheric Radiation Measurement Enhanced Shortwave Experiment (ARESE), was conducted in the fall of 1995 (Valero et al. 1997a,b) and the results presented here were taken from this experiment. For ARESE, the UAV payload was flown on an Grobe Egrett aircraft, which flew at altitudes between 3 and 13 km, generally above clouds. The second aircraft maintained its altitude below cloud level and generally below the Egrett except for occasional wingtip-to-wingtip calibration flights.

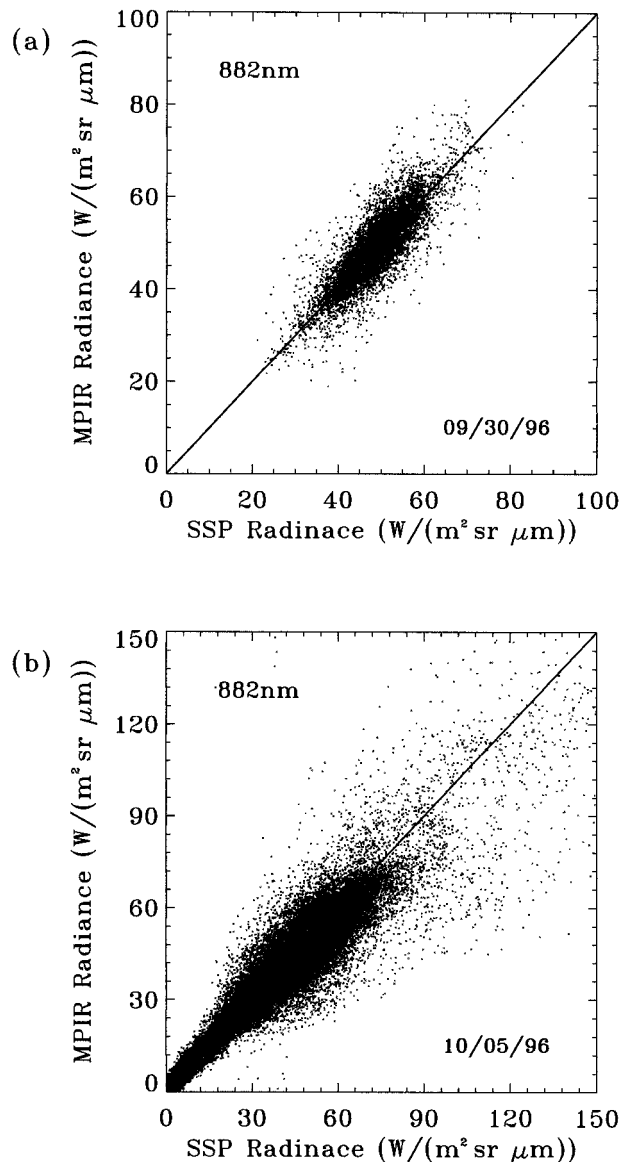


FIG. 8. Comparison of the nadir reflected radiance measured by the SSP and MPIR at 0.88  $\mu\text{m}$ .

### a. Clear-sky spectral measurements

Clear-sky spectral measurements obtained from the SSP on 11 October 1995 are presented in Fig. 9. These data were obtained during the flight of the Egrett in the vicinity of the Southern Great Plains ARM Cloud and Radiation Testbed (CART) site. On this occasion, two aircraft flew in tight formation at an altitude of about 3 km and then separated in altitude when the Egrett climbed to 13 km. The spectral fluxes measured by the SSP were averaged over a portion of the flight track when the Egrett was at an altitude of 3 km. The data are shown in Fig. 9a in the form of a spectral albedo. Since only spectrally reflected fluxes were measured, the procedure for deriving albedos from these fluxes

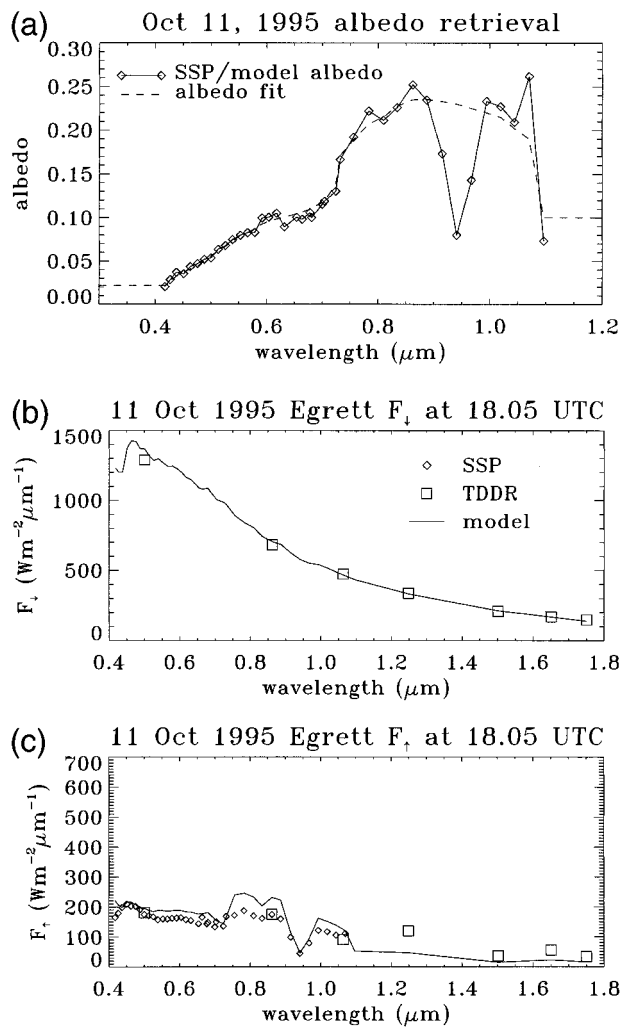


FIG. 9. (a) The clear-sky spectral albedo deduced from SSP measurements at an altitude of 3 km (solid curve) and the spectral surface albedo required to fit a model calculation to the measurements (dashed). (b) The downwelling spectral flux at the Egrett altitude of 13 km as measured by the TDDR and derived from a radiative transfer model. (c) The spectrally reflected flux at 13 km measured by the SSP and TDDR and derived from the same model used to determine the downwelling flux.

was based on the use of a spectral radiative transfer model to predict the incident spectral flux at flight altitude. The credibility of this calculated spectrum was checked using the three spectral measurements of downwelling flux available from the uplooking TDDR. The calculated downwelling spectral flux along with the measured TDDR fluxes are shown in Fig. 9b for the 13-km altitude.

The same model is combined with the SSP measurements obtained at 3-km level to derive the spectral surface albedo. The steps taken to determine this albedo include the following. (i) Simulate the spectral fluxes at the 3-km Egrett assuming a dark underlying surface and the observed atmospheric temperature and water

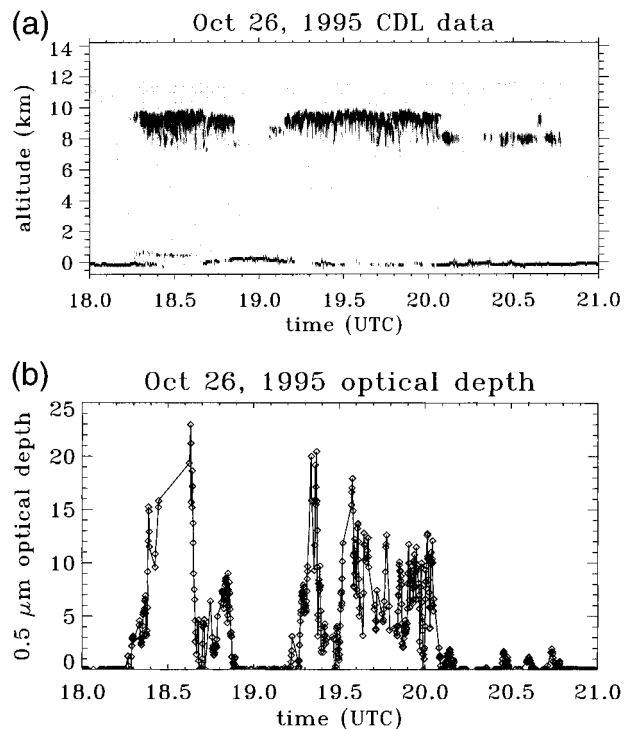


FIG. 10. (a) Time series of backscatter profiles measured by the lidar on the Egrett at 13 km on 26 Oct 1995. These profiles indicate the presence of a cirrus cloud layer located between 8 and 10 km. (b) Time series of the cirrus cloud optical depth derived from spectral radiances measured by the SSP.

vapor profile information at the time of the flights. This flux thus represents the contribution by the atmosphere between the surface and 3 km (i.e., the contribution by Rayleigh scattering and water vapor absorption). (ii) Subtract this contribution from the measured SSP fluxes. The spectral surface albedo is then related to this residual flux. The albedo determined in this way is also shown in Fig. 9a and strictly represents the albedo of the surface as well as any unaccounted for effects of scattering by the atmosphere between the aircraft at 3 km and the surface (such as due to aerosol in this layer) that is not included specifically in the model. Clearly evident in the albedo spectrum derived from measurements made at 3 km is the water band centered at 0.94  $\mu\text{m}$ , which is accounted for in the process of retrieving surface albedo.

This spectral surface albedo is then used as a boundary condition input into the model, which is then used to simulate measurement at other altitudes. Figure 9c provides an example of such a comparison. Shown is the spectrally reflected flux measured by the SSP at 13 km and the spectral flux predicted by the model using the same inputs as applied to produce the downwelling fluxes shown in Fig. 9b and the retrieved surface albedo indicated in Fig. 9a.

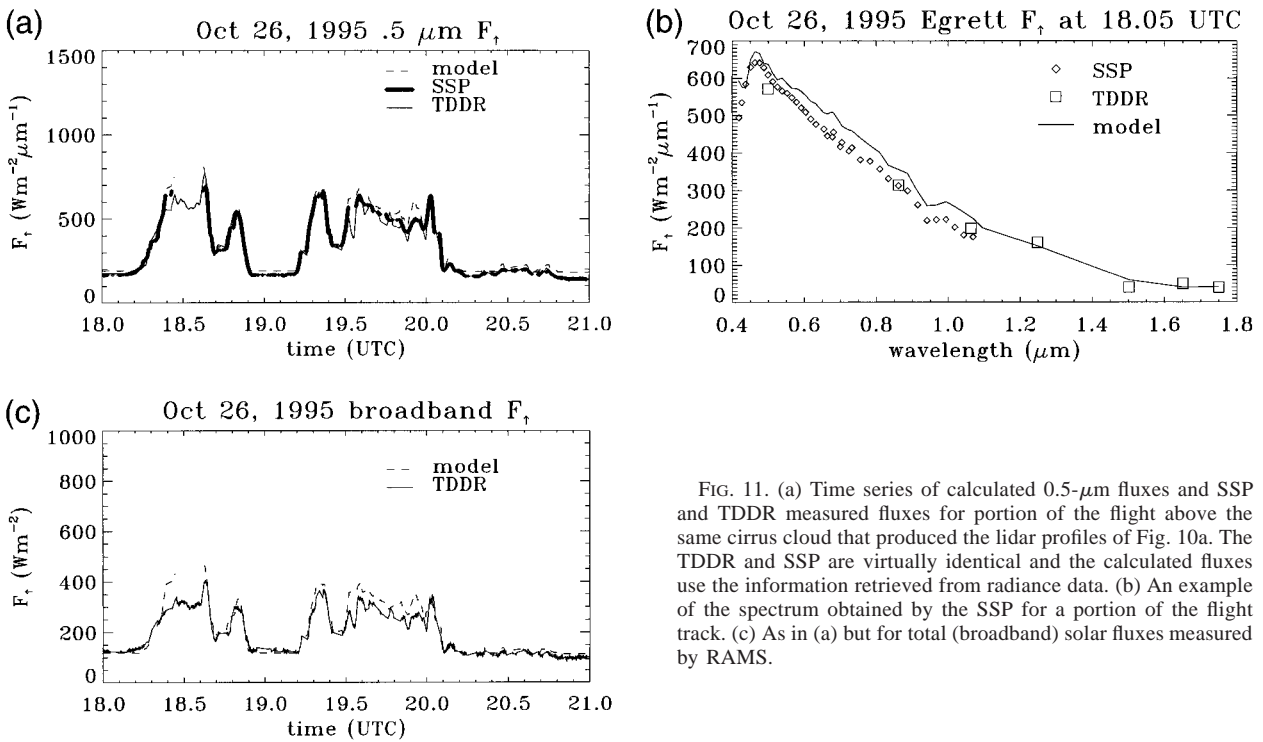


FIG. 11. (a) Time series of calculated 0.5- $\mu\text{m}$  fluxes and SSP and TDDR measured fluxes for portion of the flight above the same cirrus cloud that produced the lidar profiles of Fig. 10a. The TDDR and SSP are virtually identical and the calculated fluxes use the information retrieved from radiance data. (b) An example of the spectrum obtained by the SSP for a portion of the flight track. (c) As in (a) but for total (broadband) solar fluxes measured by RAMS.

### b. Cloudy-sky radiance and flux measurements

An example of the measured radiances and fluxes obtained for cloudy skies observed during the flight of the Egrett on 26 October is presented in Figs. 10–11. On this day, the Egrett flew a pattern above an extensive layer of cirrus cloud in the vicinity of the CART site. The characteristics of this cirrus layer are highlighted in Fig. 10a, which shows the vertical profile of lidar backscatter along the flight track of the Egrett. A relatively homogeneous cloud layer was located between 8 and 10 km with occasional low-level cloud below.

Spectral radiance data collected along the flight track of the Egrett above the cirrus were used in a cloud retrieval scheme to determine the optical depth and particle size. Details of this particular retrieval scheme is the subject of another paper (Miller et al. 2000). The time series of optical depth obtained from the radiance data are presented in Fig. 10b. The optical depth of the cloud layer varied significantly between patches that were very thin to regions where the optical thickness approached 15. The latter regions are thick enough to attenuate the lidar, as indicated by the lack of a surface return in Fig. 10a.

The mean optical depth thus obtained as well as other properties used in the retrieval scheme (such as the assumed phase function of particles) were then applied in the spectral radiative transfer model to predict spectral fluxes along the flight track of the Egrett. The calculated 0.5- $\mu\text{m}$  fluxes are compared to the SSP and TDDR 0.5- $\mu\text{m}$  measured fluxes in Fig. 11a for a selected portion

of the flight track. A single spectrum obtained by averaging data over a smaller portion of the flight track is presented in Fig. 11b. Figure 11c presents the comparison between the Radiation Measurement System (RAMS) broadband solar fluxes and the model derived solar fluxes obtained by integrating the calculated spectral fluxes to produce broadband quantities. The agreement between measured and calculated fluxes is remarkable given that no attempt was made to improve this comparison by altering particle phase functions and other parameters prescribed a priori in the retrieval.

The results presented in Fig. 11 are typical of results derived from data obtained from the majority of other flights from other experiments. The comparisons illustrate that even in the more difficult case of cirrus clouds of unknown optical properties, the spectral radiance data used to retrieve cloud properties and the spectral flux data form a consistent picture that is in reasonable agreement with model predictions. The results further show that these model predictions in turn reasonably reproduce measured broadband fluxes obtained independently with another measuring system (e.g., RAMS).

## 7. Summary and conclusions

This paper describes the design and characterization of a spectrally scanning polarimeter, which is capable of measuring spectral radiances and fluxes in the range between 0.4 and 4.0  $\mu\text{m}$ . The instrument characteristics are described including discussion of the procedures to

calibrate the unpolarized radiances and fluxes along with detailed error of this calibration. Examples of SSP measured spectral radiances and fluxes obtained from aircraft experiments carried out by the U.S. Department of Energy UAV program are described. The measurements examples are of unpolarized fluxes and radiances in the range between 0.4 and 1.1  $\mu\text{m}$ .

The field of view of the radiance channel was determined to be 20 mrad, and the angular response of the flux channel was shown to be close to the desirable cosine response at visible wavelengths at view angles less than  $60^\circ$  from instrument normal. Departures from a cosine response occur at lower angles and at longer wavelengths with the appearance of forward transmission lobes for highly anisotropic light sources (for the wavelengths longer than 740 nm and for very small range of angles, i.e., from  $-2^\circ$  to  $2^\circ$ ).

The accuracy of the calibration of radiances was determined to be approximately 3%. The calibration of fluxes, based on a procedure that places the instrument in the aperture of a 40-in. integrating sphere, varied in accuracy from 3% to 6%. The quoted calibration accuracy (in principle) applies to conditions similar to this calibration procedure, namely, the isotropic light source. In principle, uncertainties will be introduced as the light source geometry varies from an isotropic source as it does in the real atmosphere. An assessment of the likely magnitude of this uncertainty is presented through comparison with spectral flux measurements obtained from a different instrument with different angular response properties. Comparisons of reflected solar fluxes observed under a variety of conditions suggest that the uncertainty introduced by cosine response errors are relatively small and the quoted accuracies are robust, at least for the range of conditions expected when the SSP views diffusely reflected sunlight.

Measurements obtained from two different aircraft flights were also presented to illustrate the type of applications of the data. In the first example, spectral fluxes obtained along a low-level flight track of the aircraft under clear-sky conditions were used with a model of the spectral fluxes to determine the spectral albedo of the underlying surface. The second application of the data applies to overcast sky containing cirrus clouds. Spectral radiance data obtained by the SSP were used to retrieve cloud optical properties and these, in turn, were applied in a model to simulate spectral fluxes that could be compared to measured fluxes. The comparisons illustrate that even in the more difficult case of cirrus clouds of uncertain optical properties, the spectral radiance data used to retrieve cloud properties and coincident spectral flux data are consistent and in reasonable agreement with model predictions, and these model predictions in turn reasonably reproduce measured

broadband fluxes obtained independently with another measuring system.

The SSP has undergone enhancements that include the replacement of the detectors described above with a two-color detector that has a silicon element mounted over an indium arsenide infrared element. The InAs detector is also mounted on a two-stage thermoelectric cooler. This development extends the SSP spectral range of operation beyond 2.5  $\mu\text{m}$ . This new version of the instrument is currently under development, and an early version of this instrument has already been deployed in a field experiment that took place at the ARM CART site in August 1998.

*Acknowledgments.* The development of this instrument, data collection, and subsequent analyses were supported by Department of Energy Grants DE-FG-03-97ER62357 and DE-FG-03-05ER61985.

#### REFERENCES

- Barker, H., and Z. Li, 1997: Interpreting shortwave albedo–transmittance plots: True or anomalous absorption? *Geophys. Res. Lett.*, **24**, 2023–2026.
- Cess, R. D., and Coauthors, 1995: Absorption of solar radiation by clouds: Observations versus models. *Science*, **267**, 496–499.
- Chen, H. S., 1985: *Space Remote Sensing Systems, an Introduction*. Academic Press, 255 pp.
- Miller, S., G. L. Stephens, C. K. Drummond, A. K. Heidinger, and P. T. Partain, 2000: A multisensor satellite cloud property retrieval scheme. *J. Geophys. Res.*, in press.
- Pilewskie, P., and F. P. J. Valero, 1995: Direct observations of the excess solar absorption by clouds. *Science*, **267**, 1626–1629.
- Scott, J. C., and G. L. Stephens, 1985: A visible–infrared spectroradiometer for cloud reflection measurements. *J. Phys. E: Sci. Instrum.*, **18**, 697–701.
- Stephens, G. L., 1996: How much solar radiation do clouds absorb? *Science*, **271**, 1131–1133.
- , and J. C. Scott, 1985: A high speed spectrally scanning radiometer (SPERAD) for airborne measurements of cloud optical properties. *J. Atmos. Oceanic Technol.*, **2**, 148–156.
- Stokes, G., and S. Schwartz, 1994: The Atmospheric Radiation Measurement (ARM) Program: Programmatic background and design of the cloud and radiation test bed. *Bull. Amer. Meteor. Soc.*, **75**, 1201–1221.
- Valero, F. P. J., and T. P. Ackerman, 1989: The effects of the Arctic haze as determined from airborne radiometric measurements during AGASP II. *J. Atmos. Chem.*, **9**, 225–244.
- , W. J. Y. Gore, and L. P. M. Giver, 1982: Radiative flux measurements in the troposphere. *Appl. Opt.*, **21**, 831–838.
- , S. K. Pope, R. G. Ellingson, A. W. Strawa, and J. Vitko, 1996: Determination of clear-sky radiative profiles, heating rates, and optical depths using unmanned aerospace vehicles as a platform. *J. Atmos. Oceanic Technol.*, **13**, 1034–1030.
- , A. Bucholtz, B. C. Bush, S. K. Pope, W. D. Collins, P. Flatau, A. Strawa, and W. J. Y. Gore, 1997a: Atmospheric Radiation Measurements Enhanced Shortwave Experiment (ARESE): Experimental and data details. *J. Geophys. Res.*, **102**, 29 929–29 937.
- , R. D. Cess, M. Zhang, S. K. Pope, A. Bucholtz, B. Bush, and J. Vitko Jr., 1997b: Absorption of solar radiation by the cloudy atmosphere: Interpretations of collocated aircraft measurements. *J. Geophys. Res.*, **102**, 29 917–29 927.